Three-Dimensional Simulation of Bubble Column Flows with Bubble Coalescence and Breakup

P. Chen and M. P. Duduković
Chemical Reaction Engineering Laboratory, Dept. of Chemical Engineering, Washington University, St. Louis, MO 63130

J. Sanyal
Fluent Inc., Lebanon, NH 03766

DOI 10.1002/aic.10381
Published online in Wiley InterScience (www.interscience.wiley.com).

Three-dimensional (3-D) Euler/Euler simulations of two-phase (gas/liquid) transient flow were performed using a multiphase flow algorithm based on the finite-volume method. These numerical simulations cover laboratory-scale bubble columns of different diameters, operated over a range of superficial gas velocities in the churn-turbulent regime (8 to 30 cm/s) and at different operating pressures (up to 1 MPa). The bubble population balance equation (BPBE) is implemented in the two-fluid model (TFM) and algebraic slip mixture model (ASMM). Simulated time-averaged axial liquid velocity, turbulence stress, and gas holdup are compared with experimental data of Chen et al., Ong, and Shaikh et al. Moreover, to ensure the experimentally observed lack of dependency of holdup radial profiles on column height in the fully developed region, coalescence rates in the computations had to be enhanced consistently compared to model-predicted values. Quantitative agreement is then obtained between the experimental data and simulations for the time-averaged gas holdup and axial liquid velocity profiles. However, the simulations significantly underestimate the turbulent stress because the velocity field cannot be fully resolved. Simulated bubble size distributions indicate that the volume fraction of small bubbles is uniform in a cross section, whereas that of the large bubbles peaks in the center of the column. The simulation correctly captures the high-pressure effect, which at fixed gas superficial velocity pushes the bubble column flow toward bubbly flow. The simulation also predicts that, although the small bubble volume fraction may not change with superficial gas velocity in the churn-turbulent flow regime, the bubble size distribution still remains single modal but is wider and contains larger bubble sizes when superficial gas velocity is increased. © 2005 American Institute of Chemical Engineers *AIChE J,* 51: 696–712, 2005

Keywords: bubble columns, computational fluid dynamics, dynamic simulation, population balance, modeling, multiphase flow

Introduction

Bubble columns serve as multiphase contactors and reactors in the chemical, petrochemical, biochemical, and metallurgical industries, primarily because of the ease and low cost of construction, simplicity of operation, ability to handle solids, excellent heat and mass transfer characteristics, and no sealing problems arising from the absence of mechanically moving parts. In spite of the simplicity in mechanical design, fundamental properties of the two-phase fluid dynamics associated with the operation of a bubble column reactor, which are essential for scale-up and design, are still not fully understood because of the complex nature of multiphase flow.

Correspondence concerning this article should be addressed to M. P. Duduković at dudu@poly1.che.wustl.edu.

One of the primary tasks in the current methodology of bubble column design involves description of the degree of mixing of each of the involved phases (such as the axial dispersion model), which is subsequently used along with reaction kinetics to estimate the reactor performance with respect to such parameters as conversion, yield, and selectivity. The advantages of phenomenological models, using parameters obtained from transient fluid dynamic models of the column, have previously been demonstrated (Degaleesan, 1997; Degaleesan et al., 1997). Thus, the time-dependent velocity field is needed for calculating the convection and turbulent dispersion of the passive scalar in the liquid and/or gas phase.

During the last decade, the dynamic simulation of gas–liquid flow in bubble columns has drawn considerable attention of investigators in the chemical reaction engineering community. This has resulted in a number of computational fluid dynamics (CFD) studies (Delnoij et al., 1997; Krishna et al., 2000; Lapin and Lübbert, 1994; Pan et al., 2000; Sokolichin and Eigenberger, 1994; Torvik and Svendsen, 1990). However, the uncertainty regarding the various phase interaction terms and turbulence closure schemes, in addition to the computational difficulties associated with computation of large flow fields, have delayed the full implementation of CFD codes in practice. Simulation of the churn-turbulent flow regime, which is often preferred for industrial bubble columns, poses further difficulties arising from the complications that result from multiple bubble sizes and bubble interactions.

Most reported numerical studies dealt with two-dimensional (2-D) columns or used the axisymmetric 2-D approximation for cylindrical columns. Most previous studies compared their numerical predictions with experimental measurement in a qualitative way, whereas only a few quantitative comparisons were made. Therefore, although qualitative comparisons are satisfactory in general, limited conclusions regarding the validation and reliability of the numerical prediction can be drawn from these studies. It is widely recognized that the physical models used in current numerical investigations, which include the interphase momentum exchange and multiphase turbulence closures, require experimental data for verification and improvement. 3-D dynamic simulations of the highly transient gas–liquid flow in either cylindrical or rectangular bubble columns are needed. Among the recent efforts in this area, Pfleger et al. (1999) suggested that the column depth must be resolved meticulously to obtain accurate hydrodynamics in a rectangular bubble column simulation. Krishna et al. (2000) performed both 2-D axisymmetric and full 3-D simulations of bubble columns by using a gas-phase model consisting of two bubble classes, that is, small and large bubbles. The results from 3-D simulations show an improvement in the prediction of gas holdup compared with 2-D-axisymmetric simulations. Van Baten and Krishna (2001) extended the 3-D simulation to include the effect of physical properties of the continuous phase, but the main conclusions remained the same. Ranade and Tayalia (2001) investigated the influence of sparger design on the hydrodynamics of a bubble column by using the drag formulation proposed by Schwarz and Turner (1988). Their computations overpredicted the gas holdup by 90% for full 3-D simulations.

To model the drag force term, which is one of the key closures, most numerical simulations resort to a single-particle model with a so-called mean bubble size (for example, Pan et al., 2000; Sokolichin and Eigenberger, 1994). This is mostly done because modeling different sizes of bubbles as individual phases leads to unrealistic computational cost and is characterized by numerical convergence problems. Such an approach is still plausible in bubbly flow because bubble–bubble interactions are weak and the bubble sizes are narrowly distributed. However, in churn-turbulent flow, which is predominant in most industrial applications, bubble–bubble interactions result in widely distributed bubble sizes that may be substantially different from the "mean" bubble size assumption. In addition, to generate a simulation result that resembles available data, the "mean" bubble size is customarily adjusted by a trial-and-error procedure and the value so chosen often is far from reality.

There is a need, when evaluating the performance of existing bubble column reactors and when designing new ones in churn-turbulent flow, to assess the gas holdup radial distribution, because it drives liquid recirculation, and local interfacial area concentration distribution, because it is essential to mass transfer. An engineering level of accuracy is needed. Based on extensive studies by many authors, we know that the two-fluid model-based codes (such as FLUENT, CFX, CFDLib, and so on) that use the mean bubble size concept cannot predict well the observed gas holdup radial profiles, even in 3-D simulation, especially in churn-turbulent flow. The predicted velocity profiles and overall gas holdup estimates (Pan and Duduković, 2001) are reasonably good. Moreover, available estimates of the local interfacial area are based on the predicted local gas holdup and on the assumed mean bubble size and are likely in error. One of the reasons for the mismatch of the holdup profile prediction and data could be that the current simulations use the so-called *mean bubble size assumption*, which does not hold well in the churn-turbulent flow regime. To remedy this situation Krishna and coworkers (for example, Krishna et al., 2000; van Baten and Krishna, 2001) introduced a model consisting of two bubble classes, small and large, and suggested a set of rules for their interactions based on empirical evidence. Some improvement in holdup profile predictions was observed (Krishna et al., 2000). To further base the simulation on physical grounds the implementation of the bubble population balance model (BPBE) in the Eulerian/Eulerian model is needed to eliminate the assumption of single constant bubble size or of the assignment of two bubble classes. The implementation of BPBE allows one to predict the bubble size distribution locally and eliminate the trial-and-error procedure with respect to the unknown mean bubble diameter mentioned earlier, while providing the capability of predicting the interfacial area concentration locally throughout the column.

Experimental Data

At the Chemical Reaction Engineering Laboratory, Washington University in St. Louis, MO, the unique computer-automated radioactive particle tracking–computed tomography (CARPT–CT) facilities allow noninvasive monitoring of the flow of two phases in opaque multiphase reactors on a single platform (Degaleesan, 1997; Devanathan, 1991; Kumar, 1994; Yang et al., 1992). CARPT is a noninvasive technique for tracking the trajectory of a radioactive particle moving along with the continuous phase. In CARPT, one resorts to tagging the "typical fluid element" with a gamma-ray source (that is, the liquid phase is tagged with a neutrally buoyant radioactive

particle). The location of the particle that follows the liquid phase at each time instant, $\mathbf{x}_p(t)$, can be reconstructed from a record of the gamma-ray photon counts at a number of strategically located sodium iodide detectors, and a preestablished calibration between the detector counts and tracer particle location. Tracer particle trajectory is acquired over a very long time, typically 18–20 h, to collect sufficient statistics (typically, two million or more occurrences in the column). The time-averaged liquid velocities, turbulence parameters, and eddy diffusivities can be further calculated from the tracer particle trajectory (Devanathan et al., 1990).

CT is used to measure time-averaged phase holdup profiles in a vessel, such as gas holdup profiles, in a bubble column. By placing a strong gamma-ray source in the plane of interest and a planar array of collimated scintillation detectors on the other side of the reactor, one measures attenuation in the beam of gamma radiation. The attenuation is a function of the line-averaged holdup distribution along the path of the beam. Many such "projections" are obtained at different angular orientations around the reactor. The complete set of projections is then used to back-calculate the cross-sectional distribution of densities using an estimation-minimization algorithm. Because the density at any point in the cross section is a sum of densities of individual phases weighted by their volume fractions, the cross-sectional holdup distribution of any particular phase can be uniquely recovered, provided only two phases are present. The total scanning time is about 2 h; thus the scanned image provides a time-averaged cross-sectional distribution of mixture density. The results of the 2-D holdup distribution can be subsequently averaged azimuthally for direct comparison against a suitable simulation.

Details of the experimental setup and procedure for the particle tracking and the tomographic techniques can be found elsewhere (Chaouki et al., 1997; Degaleesan, 1997; Devanathan, 1991; Devanathan et al., 1990; Kumar et al., 1995, 1997; Moslemian et al., 1992; Roy, 2000; Yang et al., 1992).

Computational Models

The Eulerian multiphase model

The governing equations in this approach can be derived by ensemble averaging the fundamental conservation equations for each phase to describe the motion of liquid and gas in a bubble column. Both the continuous and the dispersed phase are modeled in the Eulerian frame of reference as interpenetrating continua. The mass and momentum balance equations are written separately for each phase. The momentum equations of the phases interact with each other through interphase momentum exchange terms. The representative contributions to the derivation of this model include studies by Drew (1983), Kashiwa and Rauenzahn (1994), Zhang and Prosperetti (1997), and Drew and Passmann (1999). The continuity equation for each phase is written as

$$\frac{\partial \alpha_k}{\partial t} + \nabla \cdot (\alpha_k \mathbf{u}_k) = 0 \tag{1}$$

where α_k and $\mathbf{u}_k$ are the volume fraction and the phase averaged velocity, respectively, of the liquid phase ($k = l$) and the gas phase ($k = g$). The momentum equation for the liquid phase is

$$\frac{\partial (\alpha_k \rho_k \mathbf{u}_k)}{\partial t} + \nabla \cdot (\alpha_k \rho_k \mathbf{u}_k \mathbf{u}_k) = -\alpha_k \nabla P + \alpha_k \rho_k \mathbf{g} \pm \mathbf{F}_{kl} + \nabla \cdot (\alpha_k \boldsymbol{\tau}_k) + \nabla \cdot (\alpha_k \rho_k \mathbf{u}'_k \mathbf{u}'_k) \tag{2}$$

where $\mathbf{g}$ is the gravity acceleration, $\mathbf{F}_{kl}$ is the interfacial momentum exchange term, and $\boldsymbol{\tau}_k$ is the viscous stress tensor, which can be expressed by

$$\boldsymbol{\tau}_k = \mu_k (\nabla \mathbf{u}_k + \nabla \mathbf{u}_k^{\mathrm{T}}) - \frac{2}{3} \mu_k \nabla \cdot \mathbf{u}_k \mathbf{I} \tag{3}$$

and $\alpha_k \rho_k \mathbf{u}'_k \mathbf{u}'_k$ is the turbulent stress tensor that must be closed by an appropriate multiphase turbulence model. Because of the loss of information in the averaging process, several correlations (such as the interfacial momentum exchange term $\mathbf{F}_{kl}$ in Eq. 2) appear in the macroscopic equations that must be closed in terms of known variables. In a recent review (Rafique et al., 2004) the various interfacial forces were discussed. The effect of added mass can be seen only when high-frequency fluctuations of the slip velocity occur (Drew, 1983). These high-frequency velocity fluctuations (such as $\mathbf{u}'_k$), however, are not resolved in the two-fluid model, and are lost in the averaging process. It has been estimated that added mass force is much smaller than the drag force (Oey et al., 2003) in bubbly flow. Even in gas–liquid stirred tank, where the velocity fluctuation is much stronger than in bubble column flows, the inclusion of added mass force has at best a "tuning effect" on the simulation (Jenne, 1999).

Mathematically, the inclusion of lift force should have a strong effect on the simulation. Oey et al. (2003) estimate that the lift force component in the transversal direction has the same order of magnitude as the corresponding drag force component, provided $C_L = 0.5$, where C_L is the lift force coefficient. However, there are a number of lift forces (such as Magnus force, Saffman force, lift force arising from bubble deformation, etc.) and there is a dispute regarding the magnitude of the lift force coefficient (Lahey, 1990) and even the sign of the dominant term (Jakobsen et al., 1997). In addition, lift arising from bubble deformation is suspected of being dominant in churn-turbulent flow and it has not yet been properly modeled for inclusion as a closure in the Euler/Euler model, and by neglecting lift force one can still achieve values that compare well with experimental data (Pan and Duduković, 2001; Pan et al., 1999, 2000). Subject to these uncertainties, and based on existing evidence that these forces are either smaller compared to drag force or not yet properly modeled, only the drag force is included, whereas the added mass force and lift force are neglected in the model for interphase momentum exchange. The drag force term is calculated by

$$\mathbf{M}_d = \frac{3}{4} \alpha_g \alpha_l \frac{\rho_l}{d_b} C_D |\mathbf{u}_l - \mathbf{u}_g| (\mathbf{u}_l - \mathbf{u}_g) \tag{4}$$

The liquid holdup, α_l, in Eq. 4 accounts for the situation of a bubble moving through a gas–liquid mixture instead of a pure liquid. With this factor, we still use the drag law for a single bubble to approximately calculate the drag coefficient, C_D (Schiller and Naumann, 1935)

$$C_D = \begin{cases} 24\left(\dfrac{1 + 0.15\ \mathrm{Re}^{0.687}}{\mathrm{Re}}\right) & \mathrm{Re} \le 1000 \\ 0.44 & \mathrm{Re} > 1000 \end{cases} \quad (5)$$

where $\mathrm{Re} = d_b|\mathbf{u}_l - \mathbf{u}_g|\rho_l/\mu_l$. By using Eqs. 4 and 5, we attempt to model the bubble–fluid momentum coupling in a very complex system where bubbles of various sizes and shapes exist by assuming that the local mean diameter of the bubbles, which varies with time and position and can be obtained from the bubble population balance equation (BPBE), describes the effect caused by multibubble interaction. It should be noted that there are several drag coefficient correlations for a gas–liquid system (for example, Ishii and Zuber, 1979; Tsuchiya et al., 1997) developed from a single bubble rising in quiescent liquid or in dilute bubbly flows. However, if they are applied to a churn-turbulent flow regime, these correlations significantly overestimate the drag coefficient so that one has to artificially increase the bubble size for simulations to match observed flow data. For example, when the correlation proposed by Tsuchiya et al. (1997) is used to calculate the drag force, the mean bubble size of 32 mm is assigned (from experimentally observed ~7 mm) to fit the liquid axial velocity profile in a 0.44-m-diameter air–water column operated at $U_g = 0.10$ m/s (Pan and Duduković, 2000).

The above widely used drag formulation of Eq. 4 does not take the elevated pressure into account. Krishna and van Baten (2001) proposed to use a density correction factor, $\rho_g/\rho_{g,1\mathrm{atm}}$, in the drag formulation for large bubbles based on Kelvin–Helmholtz stability analysis performed by Letzel et al. (1998). However, the introduction of such correction factor significantly overpredicted the overall gas holdup at higher superficial velocity and higher pressure (Krishna and van Baten, 2001). One possible reason is that turbulence and wake entrainment, rather than Rayleigh–Taylor and Kelvin–Helmholtz instability, are dominant in a churn-turbulent flow regime. Thus, the density correction factor is reduced in this work to $(\rho_g/\rho_{g,1\mathrm{atm}})^{0.25}$ and the drag force term in this work is calculated by

$$\mathbf{M}_d = \frac{3}{4}\alpha_g\alpha_l\frac{\rho_l}{d_b}C_D\left(\frac{\rho_g}{\rho_{g,1\mathrm{atm}}}\right)^{0.25}|\mathbf{u}_l - \mathbf{u}_g|(\mathbf{u}_l - \mathbf{u}_g) \quad (6)$$

The full justification of this density ratio factor will have to come eventually from theory or additional experimental confirmation.

The local mean bubble diameter is an important needed input parameter for the simulation. It can be estimated from former experience or by a trial-and-error method, calculated from available mean bubble diameter correlations, or obtained from the bubble population balance equation as discussed briefly in the next section.

In the two-fluid model, the turbulence in the liquid phase is modeled through a set of modified k–ε equations with extra terms that include interphase turbulent momentum transfer (Elghobashi and Abou-Arab, 1983; Launder and Spalding, 1974). For the dispersed gas phase, the turbulence closure is generated through correlations from the theory of dispersion of discrete particles by homogeneous turbulence (Tchen, 1947). The details of the modified k–ε model implementation can be found elsewhere (FLUENT manual).

The algebraic slip mixture model (ASMM)

The algebraic slip mixture model assumes that there is no interface between the two immiscible phases, that is, it allows the phases to be completely interpenetrating. The volume fractions α_1 and α_2 in a control volume can therefore be equal to any value between 0 and 1, depending on the space occupied by either phase. Moreover, the algebraic slip mixture model allows the two phases to move at different velocities. In this model one solves the continuity equation for the mixture phase, the momentum equation for the mixture phase, and the volume fraction equation for the secondary phase, as well as an algebraic expression for the relative velocity. The continuity equation for the mixture phase can be written as

$$\frac{\partial\rho_m}{\partial t} + \nabla\cdot(\rho_m\mathbf{u}_m) = 0 \quad (7)$$

where $\rho_m = \sum_{k=1}^{n}\alpha_k\rho_k$ is the mixture density and $\mathbf{u}_m = (\sum_{k=1}^{n}\alpha_k\rho_k\mathbf{u}_k)/\rho_m$ is the mass-averaged mixture velocity. The momentum equation for the mixture can be obtained by summing the individual momentum equations for the two phases. It can be written as

$$\frac{\partial(\rho_m\mathbf{u}_m)}{\partial t} + \nabla\cdot(\rho_m\mathbf{u}_m\mathbf{u}_m) = -\nabla p + \nabla\cdot(\boldsymbol{\tau}_m + \boldsymbol{\tau}_m^t) + \nabla\cdot\boldsymbol{\tau}_{Dm} + \rho_m\mathbf{g} \quad (8)$$

where $\mu_m = \sum_{k=1}^{n}\alpha_k\mu_k$ is the mixture viscosity; $\mathbf{g}$ is the gravity acceleration; and $\boldsymbol{\tau}_m$, $\boldsymbol{\tau}_m^t$, and $\boldsymbol{\tau}_{Dm}$ are the mixture viscose stress, turbulent stress, and diffusion stress attributed to the phase slip, respectively, defined as

$$\boldsymbol{\tau}_m = \mu_m(\nabla\mathbf{u}_m + \nabla\mathbf{u}_m^{\mathrm{T}}) - \frac{2}{3}\mu_m\nabla\cdot\mathbf{u}_m\mathbf{I} \quad (9)$$

$$\boldsymbol{\tau}_m^t = \mu_m^t\left[(\nabla\mathbf{u}_m + \nabla\mathbf{u}_m^{\mathrm{T}}) - \frac{2}{3}\nabla\cdot\mathbf{u}_m\mathbf{I}\right] - \frac{2}{3}\rho_m k_m\mathbf{I} \quad (10)$$

$$\boldsymbol{\tau}_{Dm} = \sum_{k=1}^{m}\alpha_k\rho_k\mathbf{u}_{D,k}\mathbf{u}_{D,k} \quad (11)$$

where k_m is the mixture turbulent kinetic energy density, $\mathbf{u}_{D,k} = \mathbf{u}_k - \mathbf{u}_m$ represents the drift (diffusion) velocities for liquid and gas phases with respect to the mass center, respectively. The turbulent stress term in the mixture equation is closed by solving a standard k–ε model for the mixture phase. The slip velocity is defined as the velocity of the secondary phase relative to the primary phase velocity

$$\mathbf{u}_{slip} = \mathbf{u}_2 - \mathbf{u}_1 \quad (12)$$

The slip velocity and the drift velocity are related by the following expression

$$\mathbf{u}_{D,2} = \mathbf{u}_{slip} - \sum_{i=1}^{n} \frac{\alpha_i \rho_i \mathbf{u}_{1i}}{\rho_m} \tag{13}$$

The basic assumption of the ASMM, required to prescribe an algebraic relation for the slip velocity, is that a local equilibrium between the phases is reached over short spatial length scales. This implies that the accelerating dispersed phase particles/bubbles attain the terminal velocity after traveling a distance that is much smaller than the length scale of the system. The form of the slip or relative velocity is given by

$$\mathbf{u}_{slip} = \tau_{12}\mathbf{a} \tag{14}$$

where $\mathbf{a}$ is the dispersed phase particle acceleration and τ_{12} is its relaxation time. If the particle/bubble is small compared to the scale of the velocity variations and possesses a low-particle Reynolds number, it follows the motion of the fluid. According to Clift et al. (1978), a particle follows the fluid motion if its relaxation time τ_{12} is small compared with the hydrodynamic timescale. In the Stokes regime this condition can be written as

$$\tau_{12} = \frac{\rho_2 d_p^2}{18\mu_m} \ll \tau_{hydro} \tag{15}$$

where d is the particle (bubble) diameter and τ_{hydro} is the hydrodynamic time scale of the system. From the continuity equation of the secondary (dispersed) phase one can obtain the volume fraction equation for the secondary phase

$$\frac{\partial}{\partial t}(\alpha_s \rho_s) + \nabla(\alpha_s \rho_s \mathbf{u}_m) = -\nabla \cdot (\alpha_s \rho_s \mathbf{u}_{D,s}) \tag{16}$$

Bubble population balance equation (BPBE)

In bubble column reactors, the initial bubble size is determined by the formation of bubbles at the sparger. However, this initial bubble size may not be stable because of turbulence, interfacial instability, wake entrainment, size dependent rise velocity difference, and shear layer–induced velocity difference. In all these cases, the bubble size is further determined by a breakup and/or coalescence mechanism. In reaction systems, in addition to the breakup and coalescence, mass transfer should also been considered. Phase change and pressure change may also need to be taken into account.

Because the interfacial area concentration changes with the variation in the bubble number density as a result of coalescence and breakup, analogous to Boltzmann's transport equation, a population balance model can be used to provide a statistical formulation to describe the dispersed phase in a multiphase flow. Generally, the population balance equation can be expressed as

$$\frac{\partial}{\partial t} f(\mathbf{x}, \nu, t) + \nabla \cdot [\mathbf{u}_b(\mathbf{x}, \nu, t) f(\mathbf{x}, \nu, t)] = S(\mathbf{x}, \nu, t) \tag{17}$$

In this equation $f(\mathbf{x}, v, t)$ is the bubble number density function, which is assumed to be continuous and specifies the probable number density of bubbles at a given time t, in the spatial range $d\mathbf{x}$ about a position $\mathbf{x}$, with bubble volumes between v and $v + dv$. $\mathbf{u}_b(\mathbf{x}, v, t)$ is the local velocity of bubble volumes between v and $v + dv$ at time t. $S(\mathbf{x}, v, t)$ is the source term which can be expressed as

$$\begin{aligned} S(\mathbf{x}, \nu, t) = {} & \frac{1}{2}\int_0^{\nu} a(\nu - \nu', \nu') f(\mathbf{x}, \nu - \nu', t) f(\mathbf{x}, \nu', t) d\nu' \\ & - f(\mathbf{x}, \nu, t) \int_0^{\infty} a(\nu, \nu') f(\mathbf{x}, \nu', t) d\nu' \\ & + \int_{\nu}^{\infty} m(\nu') b(\nu') P_d(\nu, \nu') f(\mathbf{x}, \nu', t) d\nu' - b(\nu) f(\mathbf{x}, \nu, t) \\ & + S_{ph} + S_p + S_r + \cdots \end{aligned} \tag{18}$$

where the first term is the birth rate of bubbles of volume v stemming from the coalescence of bubbles of volume $v - v'$ and v'; the second term is the death rate of bubbles of volume v resulting from coalescence with other bubbles; the third term is the birth rate of bubbles of volume v resulting from breakup of bubbles with volume larger than v; and the fourth term is the death rate of bubbles of volume v arising from breakup. In addition, S_{ph}, S_p, and S_r are the bubble source/sink terms attributed to phase change, pressure change, and reaction, respectively; $a(v, v')$ is the coalescence frequency between bubbles of volume v and v'; $b(v)$ is the breakup frequency of bubbles of volume v; $m(v')$ is the mean number of daughter bubbles produced by breakup of a parent bubble of volume v'; and $P(v, v')$ is the p.d.f. of daughter bubbles produced upon breakup of a parent bubble with volume v'. It is clear that the source term needs to be closed by modeling the bubble breakup and coalescence.

In the present implementation of BPBE in the two-fluid model, all the bubbles are assumed to move at identical velocity, which equals the local ensemble-averaged gas phase velocity, $\mathbf{u_g}$, obtained from the solution of the two-fluid model. From two-fluid model equations, one can theoretically solve the continuity and momentum equation of N gas phases (N equals to the number of distinct bubble sizes to be tracked) and the liquid phase. However, it is very difficult, if not impossible, to get a large number of highly nonlinear momentum equations to converge in a realistic period of time [such as $2(N + 1)$ equations in 2-D and $3(N + 1)$ in 3-D]. To circumvent the problem of solving momentum equations for $N + 1$ separate phases, only the continuity and momentum equations for two phases (gas and liquid) are solved, as shown below. The gas phase is discretized into n subclasses according to bubble size. The number density–based population balance equation for the ith bubble class can be written as

$$\frac{\partial}{\partial t} n_i + \nabla \cdot (\mathbf{u_{bi}} n_i) = S_i \tag{19}$$

One can also derive the volume fraction based population balance equation for the ith bubble class

$$\frac{\partial}{\partial t}\alpha_i + \nabla\cdot(\mathbf{u_{bi}}\alpha_i) = S_i' \tag{20}$$

where n_i is ith bubble class local number density, α_i is ith bubble class local holdup, and $\mathbf{u_{bi}}$ is the ith bubble local velocity vector. Reaction and phase change are neglected in the present work and the source term stemming from pressure change is neglected as well. Therefore, the source term S_i or S_i' is attributed only to breakup and coalescence of bubbles and its closures will be discussed briefly later.

Either Eq. 19 or Eq. 20 is solved along with the two-fluid model in a sequential manner to obtain for each bubble class its local number density n_i. The local mean bubble size, which is needed to calculate the drag force, is given as

$$d_b = \frac{\sum_{i=1}^{N} n_i d_i^3}{\sum_{i=1}^{N} n_i d_i^2} \tag{21}$$

The aforementioned strategy can also be applied to the implementation of BPBE in the ASMM. However, contrary to the two-fluid model, only one momentum equation (the mixture momentum equation) needs to be solved in the ASMM. Therefore, the aforementioned divergence challenge does not exist, and the simplification—that all the bubbles are assumed to move at identical velocity—is not necessary. One can solve the flow field for $N + 1$ phases in the ASMM by the following modification of the volume fraction equation for the secondary phases (Eq. 16)

$$\frac{\partial}{\partial t}(\alpha_i\rho_s) + \nabla(\alpha_i\rho_s\mathbf{u}_m) = -\nabla\cdot(\alpha_i\rho_s\mathbf{u}_{D,i}) + \rho_s S_i' \tag{22}$$

Thus, different bubble class velocities are calculated (that is, the velocities of different size bubble classes are different based on their size). All three implementations described above: (1) BPBE in two-fluid model with velocities of all bubbles assumed to be locally equal to gas-phase ensemble local averaged velocity; (2) BPBE in ASMM with velocities of all bubbles assumed to be locally equal to gas-phase ensemble local averaged velocity (ASMM, SV); and (3) BPBE in ASMM with N gas phases (that is, N bubble classes) and one liquid phase such that different size bubbles have different local velocity calculated from ASMM (ASMM, DV), are executed and discussed in this work.

Models for breakup and coalescence

For binary breakup, the kernel as given by Luo and Svendsen (1996) is

$$\mathbf{\Omega}_B(v_i : vf_{BV}) = c_B(1-\alpha_g)n_i\left(\frac{\varepsilon}{d^2}\right)^{1/3}\int_{\xi_{\min}}^{1}\frac{(1+\xi)^2}{\xi^{11/3}} \times \exp\left(-\frac{12c_f\sigma}{\beta\rho_c\varepsilon^{2/3}d^{5/3}\xi^{11/3}}\right)d\xi \tag{23}$$

where $\mathbf{\Omega}_B(v : vf_{BV})$ is the breakup rate per unit volume of continuous phase ($m^{-3}\ s^{-1}$) of a parent bubble with volume v into a daughter bubble with volume vf_{BV}, f_{BV} is the volume fraction of one daughter bubble, c_f is defined as the ratio of increased surface area with respect to the surface area of parent bubble (that is, $c_f = f_{BV}^{2/3}{}^{zsxx\ +\ (1\ -\ f_{BV})^{2/3}} - 1$), $\xi = \lambda/d$, and λ is the arriving eddy size.

This model predicts the breakup rate for original bubbles of a given size at a given combination of the daughter bubble sizes, and thus does not need a predefined daughter bubble size distribution. The daughter bubble size distribution is a result that can be calculated directly from the model.

The coalescence model is divided into two parts, the collision frequency and the coalescence efficiency. The collision rate of bubbles per unit volume θ_{ij} ($m^{-3}\ s^{-1}$), as given by Saffman and Turner (1956), can be written as

$$\theta_{ij} = \frac{\pi}{4}(d_i + d_j)^2 n_i n_j(\varepsilon d_i)^{1/3}[1 + (d_i/d_j)^{-2/3}]^{1/2} \tag{24}$$

The coalescence efficiency (dimensionless) is proposed by Luo (1993) as

$$P_C(d_i, d_j) = \exp\left\{-c\frac{[0.75(1+\xi_{ij}^2)(1+\xi_{ij}^3)]^{1/2}}{(\rho_d/\rho_c + \gamma)^{1/2}(1+\xi_{ij})^3}\mathrm{We}_{ij}^{1/2}\right\} \tag{25}$$

where $\mathrm{We}_{ij} = \rho_c d_i \bar{u}_{ij}^2/\sigma$, $\xi_{ij} = d_i/d_j$, $\bar{u}_{ij} = (\bar{u}_i^2 + \bar{u}_j^2)^{1/2} = \bar{u}_i(1 + \xi_{ij}^{-2/3})$, and $\bar{u}_i = \beta^{1/2}(\varepsilon d_i)^{1/2}$.

The coalescence rate Ω_C ($m^{-3}\ s^{-1}$) then can be written as the product of collision frequency and coalescence efficiency

$$\Omega_C = \theta_{ij}P_C(d_i, d_j) \tag{26}$$

The basic idea, in discretizating the bubble population balance equations, is that bubbles in a size range, say R_i, are assigned to a pivotal size x_i. However, breakup and coalescence processes may produce bubbles that are *between* such pivotal sizes (except in the case of a uniform linear grid, that is, $x_i = iv_{min}$) and must be reassigned to the pivots (see Figure 1). The reassignment must be done carefully to preserve the accurate calculation of selected moments of the p.d.f. Kumar and Ramkrishna (1996) proposed the following way to preserve any selected moments. For $x_i \le v < x_{i+1}$, let the fraction of bubbles of size v assigned to x_i be denoted by $\gamma_i^{(i)}$, and a fraction of $\gamma_{i+1}^{(i)}$ be assigned to size x_{i+1}. The reassignment will preserve the rth moment, provided that

$$\gamma_i^{(i)}(v)x_i^r + \gamma_{i+1}^{(i)}(v)x_{i+1}^r = v^r \qquad \text{for } r = r_1, r_2 \tag{27}$$

The above equations (that is, Eq. 27 for $r = r_1$ and $r = r_2$) yield a unique solution for the quantity $\gamma_i^{(i)}(v)$. In the present work, r was set to 0 and 1 to preserve the mass balance and the number balance, respectively. Then the source term for Eq. 19 may be written as

$$S_i(\vec{x}, t) = \sum_{x_{i-1}\le(x_j+x_k)\le x_i}^{j\ge k}\left(1 - \frac{1}{2}\delta_{jk}\right)$$

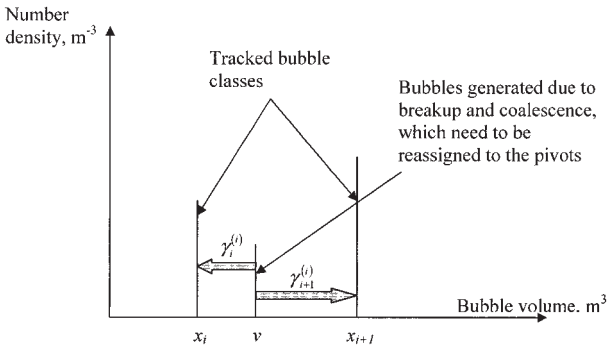

Figure 1. Bubble reassignment to pivots.

$$\times [\gamma_i^{(i-1)}(x_j + x_k)a(x_k, x_j)N_jN_k] + \sum_{x_i \le (x_j+x_k) \le x_{i+1}}^{j \ge k} \left(1 - \frac{1}{2}\delta_{jk}\right)$$

$$\times [\gamma_i^{(i)}(x_j + x_k)a(x_k, x_j)N_jN_k] - N_i \sum_{j=0}^{M} a(x_i, x_j)N_j$$

$$+ \sum_{j=i}^{M} N_j m(x_j) b(x_j) \pi_{i,j} - b(x_i)N_i \quad (28)$$

where $\pi_{i,j} = \int_{x_{i-1}}^{x_i} \gamma_i^{(i-1)}(v)P(v, x_j)dv + \int_{x_i}^{x_{i+1}} \gamma_i^{(i)}(v)P(v, x_j)dv$ and N_i (m^{-3}) is the number density of the ith bubble class.

It was found that the choice of available bubble breakup and coalescence closures does not have an important impact on the simulated results (Chen et al., 2005). Thus only breakup and coalescence closures mentioned above are implemented in this work.

Results and Discussion

Figure 2 shows a typical mesh system used for a cylindrical column. FLUENT 6 uses an unstructured mesh system consisting of hexahedral, tetrahedral, pyramid, and wedge cells. In the axial direction (z-direction), the grid is uniform. The grid sizes for each simulation are listed in Table 1. To seek a comparison with experimental data, we set the conditions for our simulations to those in experiments (Chen et al., 1999; Ong, 2003; Shaikh et al., 2003). Chen et al. (1999) measured the gas holdup distribution, liquid velocity profile and liquid phase turbulence properties in a 44-cm-diameter air–water bubble column operated at $U_g = 10$ cm/s, $P = 0.1$ MPa; Shaikh et al. (2003) measured the gas holdup distribution in a 16.2-cm-diameter air–Therminol–glass beads slurry bubble column operated at $U_g = 8$ and 14 cm/s, $P = 0.1$ MPa; and Ong (2003) measured the gas holdup distribution, liquid velocity profile, and liquid phase turbulence properties in a 16.2-cm-diameter air–water bubble column operated at $U_g = 30$ cm/s, $P = 1$, 4, and 10 atm. The column size, operating conditions, and sparger details that are needed to calculate the bubble diameter at the distributor and the corresponding computational parameters are also listed in Table 1. Initially the column is filled with liquid (or slurry, which is considered pseudo-homogeneous) (that is, $\alpha_l = 1$; $\alpha_g = 0$) up to the level that matches the static liquid height in the experiment. Above this level, the initial condition is $\alpha_l = 0$; $\alpha_g = 1$. To prevent liquid escape from the column (because no net liquid flow is used), the computational domain in the axial direction is about 50 to 80% higher than the static liquid height. The gas is introduced at all the computational cells of bottom of the column that allows only the gas phase to pass through. Because it is impossible (and it is not necessary) to resolve the gas injectors used in the experiments (such as, 0.7- to 1.32-mm-diameter holes on perforated plate) with the currently used mesh, the gas is introduced uniformly over the bottom plane (that is, in all bottom cells). The no-slip condition is used at the column wall. Finally, the pressure condition, that is, the operation pressure p, is imposed on the top of the column.

All simulations start from a static initial condition where most of the column is filled with water except for the top part, which contains only with gas. Gas is introduced at the bottom and simulations are performed until a quasi-steady state is reached. During this stage of simulation, the level of the interface is monitored. An indication of the quasi-steady state is a dynamically stabilized interface. We also monitor the velocities, both for gas and liquid phase, at some representative points in the column, as indications of flow development. Generally it takes about 60–100 s for the simulation to reach the quasi-steady state, depending on the superficial gas velocity as well as the diameter of the column. Once the fully developed, quasi-steady state is reached, the time-averaged quantities are calculated. In all simulations the velocity and gas holdup fields are sampled every 0.05–0.1 s. To ensure the convergence of the averaged quantities, the averaging processes are performed for 80–120 s. The spatial averaging is

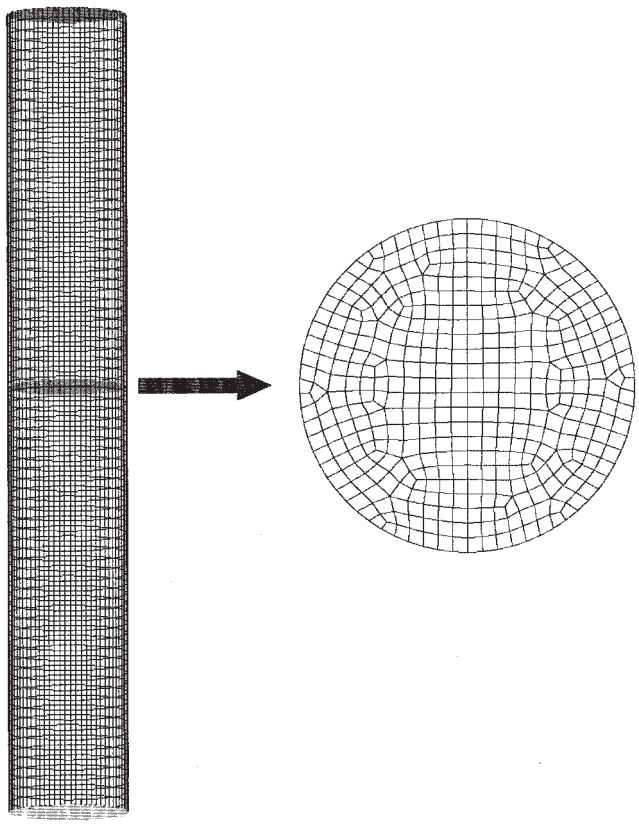

Figure 2. Typical numerical mesh.

Table 1. Column Size, Operating Conditions and the Corresponding Computational Parameters

D_c (cm)	U_g (cm/s)	System	P (MPa)	Overall Gas Holdup			Sparger Information		Δx, Δy (cm)	Δz (cm)
				Exp.	Sim.	Error%	Porosity	Hole Size (mm)		
16.2	8	Air–Therminol	0.1	0.157	0.165	5.1	0.05%	1.32	1.0	2.0
	14	Air–Therminol	0.1	0.229	0.218	−4.8	0.05%	1.32	1.0	2.0
16.2	30	Air–Water	0.1	0.267	0.284	6.4	0.15%	1.25	1.0	2.0
	30	Air–Water	0.4	0.326	0.325	−0.3	0.15%	1.25	1.0	2.0
	30	Air–Water	1.0	0.427	0.437	2.3	1.0%	1.25	1.0	2.0
44	10	Air–Water	0.1	0.191	0.162	−15.2	0.077%	0.7	2.0	3.0

then performed along the vertical direction within the middle sections of the column.

In initial simulations based on the conditions studied by Chen et al. (2005) it was consistently found that the bubble size distribution does not reach a stationary form as model-predicted coalescence and breakup rate were used. The flow field kept changing as one moved up the column, contrary to experimental evidence. This is caused by the fact that the predicted coalescence rate is about one order of magnitude higher than the predicted breakup rate calculated from the original breakup closure. However, in the churn-turbulent flow regime, the breakup and coalescence phenomena should ensure establishment of equilibrium in the fully developed region, a couple of diameters above the distributor (George et al., 2000; Ong, 2003; Shollenberger et al., 2000). Predicted breakup rates are thus enhanced in the computation in BPBE by a factor of 10 (that is, $\Omega_B = 10.0\Omega_B^{original}$) in all the simulations. It is important to emphasize that this factor is a rough engineering estimate and one could obtain "better" comparison with observed data by tweaking this factor. By doing so, however, one loses the predictive nature of CFD, which is one of the main purposes of numerical simulation. Thus, the factor by which breakup is enhanced remains 10 for all the cases considered in this work. On the other hand, the mismatch in magnitude of available breakup and coalescence closures indicates that these closures need to be reconsidered and developed further. The most likely reason for underprediction of breakup rates, which is proportional to $\varepsilon^{1/3}$, is that the k–ε model underpredicts the energy dissipation rate ε. Thus, a better turbulence model should be studied in the future.

Bubbles from 1.0 to 40.0 mm diameter are divided into nine classes (see Table 2). The bubble diameter at the sparger (that is, boundary condition for BPBE) is assumed to be uniform and is calculated from the correlation proposed by Miyahara et al. (1983), which can be written as

$$d_s = f(N_w)/(g\rho_l/\sigma d_h)^{1/3} \tag{29}$$

where

$$f(N_w) = 2.9 \qquad N_w \le 1$$

$$f(N_w) = 2.9N_w^{-0.188} \qquad 1 < N_w \le 2$$

$$f(N_w) = 1.8N_w^{0.5} \qquad 2 < N_w \le 4$$

$$f(N_w) = 3.6 \qquad 4 < N_w$$

$$N_w = \mathrm{We/Fr}^{1/2} = \frac{d_o^{1.5}U_{gh}\rho_l g^{0.5}}{\sigma}$$

The gas–liquid flow in bubble columns is highly transient and turbulent. Figure 3 shows the instantaneous isosurfaces of the gas volume fraction in columns of different diameters and operated at different superficial gas velocities and/or operating pressure. The plots show the 3-D spiral structures and transient pockets of high gas volume fraction mixtures rising up continuously in the center region of the column, carrying the surrounding liquid phase upward at higher speeds. Figure 4 illustrates typical simulated local gas holdup and liquid axial velocity time series. It can be seen that, although the flow is quite chaotic, the simulated gas holdup and liquid axial velocity oscillation is in-phase. The numerical predictions are further compared quantitatively with the experimental data.

Figure 5 shows the comparison of the simulated and experimental time-and-azimuthally averaged axial liquid (water) velocity profiles and gas holdup profile in a 44-cm-diameter column at $U_g = 10$ cm/s superficial gas velocity. The simulated results are axially averaged in the fully developed region (from $z = 89$ cm to $z = 170$ cm). Three types of models (closure implementations) mentioned earlier are implemented:

(1) BPBE in two-fluid model with velocities of all bubbles assumed to be locally equal to the gas phase ensemble local averaged velocity.

(2) BPBE in ASMM with velocities of all bubbles assumed to be locally equal to gas-phase ensemble local averaged velocity (ASMM, SV).

(3) BPBE in ASMM with $N + 1$ phases, such that different size bubbles have different local velocity calculated from the ASMM (ASMM, DV).

The simulated profiles are compared to data for the middle section of the column where the mean flow is one-dimensional.

Table 2. Bubble Classes Tracked in Simulation

	Class Index								
	1	2	3	4	5	6	7	8	9
Bubble diameter (mm)	1.00	1.60	2.50	4.00	6.35	10.08	16.00	25.40	40.00

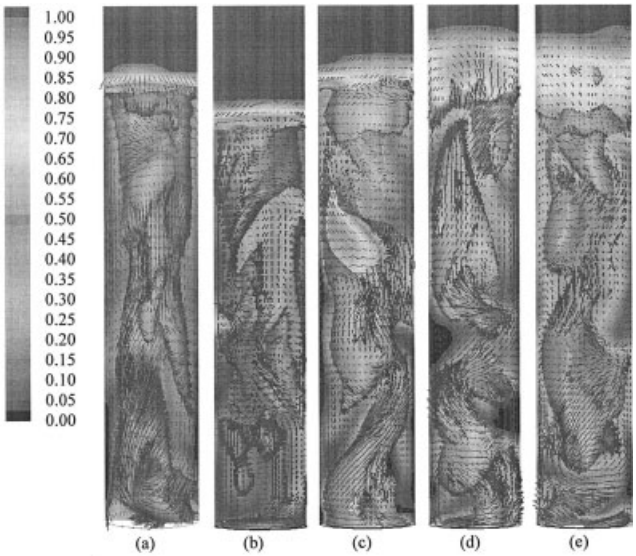

Figure 3. Instantaneous isosurfaces of the gas holdup, ε_g, in various bubble columns.

(a) $\alpha = 0.2$, $U_g = 10.0$ cm/s, (b) $\alpha = 0.13$, $U_g = 14.0$ cm/s, (c) $\alpha = 0.28$, $U_g = 30.0$ cm/s, $P = 0.1$ MPa, (d) $\alpha = 0.35$, $U_g = 30.0$ cm/s, $P = 0.4$ MPa, (e) $\alpha = 0.44$, $U_g = 30.0$ cm/s, $P = 1.0$ MPa.

The time-and-azimuthally averaged gas holdup profile *and* liquid axial velocity profile are well predicted for all three types of implementations, especially with closure types (1) and (3). The choice of the multiphase flow model and of PBM closure method does have some but not a significant effect on the simulated results, as illustrated in Figure 5. Gas holdup radial profile prediction with closure type (3) (bubbles with different velocities in ASMM) is a little lower and closer to the observed CT data than that of closure type (2) (bubbles with identical velocity in ASMM). Time-averaged liquid velocity radial profile prediction with closure type (3) is a little steeper and closer to the CARPT data than that with closure type (2). The effect of the choice of PBM closure is not significant. Besides, it is easier to implement different drag laws and pressure effects in the two-fluid model. Therefore, in what follows, only the results of the two-fluid model are presented.

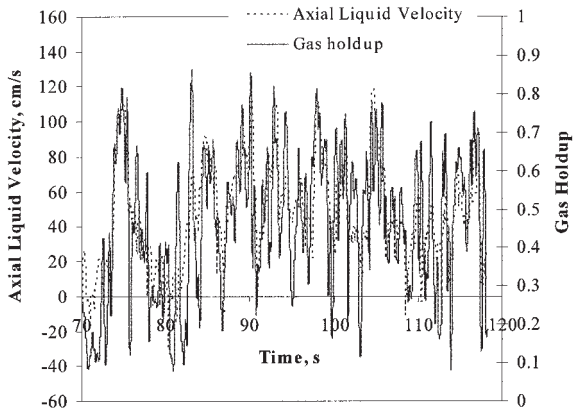

Figure 4. Typical simulated gas holdup and liquid axial velocity time series.

$D_C = 16.2$ cm, $U_g = 30.0$ cm/s, $P = 0.1$ MPa.

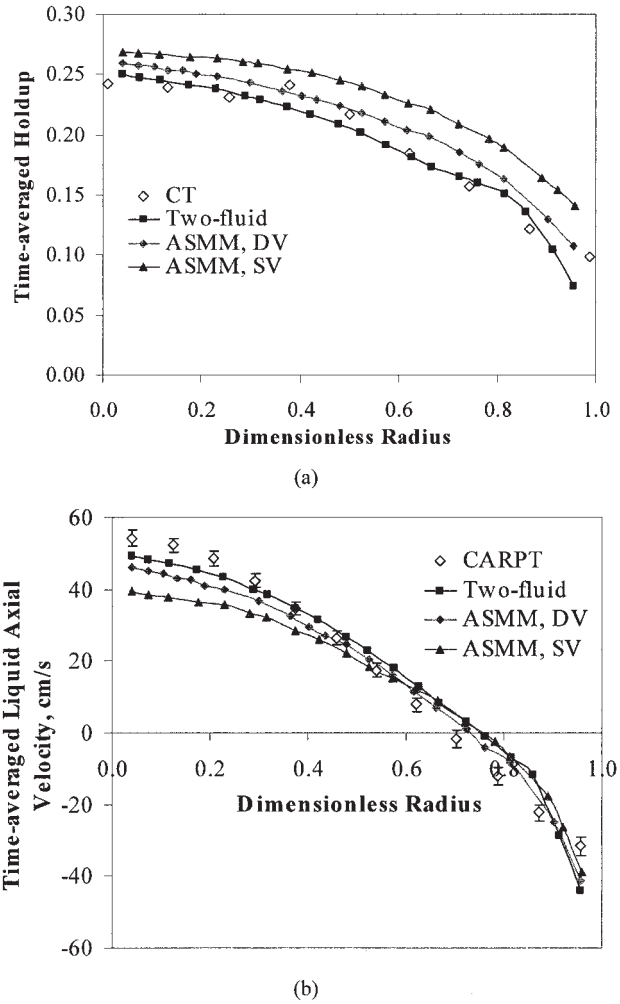

Figure 5. Comparison of time-averaged (a) axial liquid velocity and (b) gas holdup distribution with experimental data (Chen et al., 1999) measured by CT technique for air–water bubble column.

$D_C = 44$ cm, $U_g = 10.0$ cm/s, $P = 0.1$ MPa.

In the open literature, the simulated liquid axial velocity radial profiles are normally shown without exact axial location specified, and are believed to reach a plateau in the fully developed region. For 2-D axisymmetric simulation, such a plateau does exist, as illustrated in Figure 6a. However, such a perfectly flat plateau is not found in 3-D simulation. Moreover, the liquid axial velocity evolution trend obtained from 2-D and 3-D simulations are significantly different. Before reaching the plateau, the liquid axial velocity obtained from 2-D simulation exhibits a strong overshoot, which is not observed experimentally (Degaleesan, 1997), whereas the trend obtained from 3-D simulation qualitatively agrees with the experimental observations (see Figure 7). The 2-D simulation overpredicted liquid axial velocity at the centerline in the fully developed region by about 5% and 3-D simulation underpredicted it by about 5%. Figure 6b illustrates the time-averaged liquid axial velocity profile evolution in the fully developed region obtained from the 3-D simulation. The

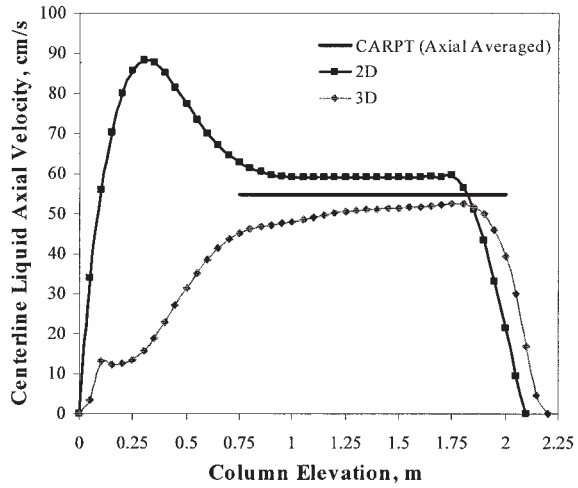

(a)

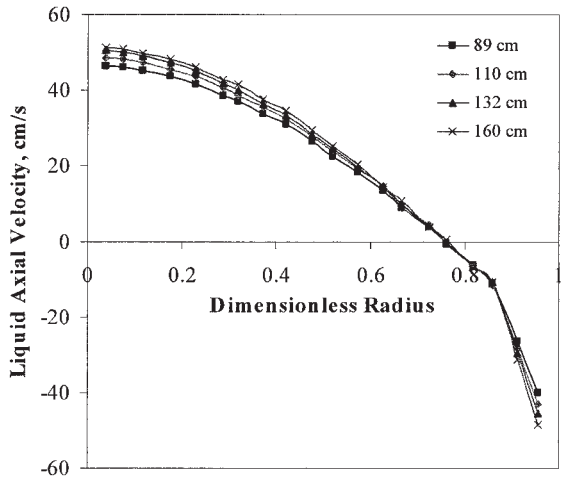

(b)

Figure 6. Time-averaged liquid axial velocity profile evolution.

variation is not significant (±5%), although the trend is apparent. Similarly for the simulated gas holdup profile, there is small variation (±5%) at different axial locations in the fully developed region, as illustrated in Figure 8.

Figure 9 shows the time-and-azimuthally averaged gas holdup profile in a 16.2-cm-diameter column operated at U_g = 8 and 14 cm/s in an air–Therminol–glass beads (150 μm) slurry system. The solids loading is 9.1%. The slurry phase is assumed to be pseudo-homogeneous, thus two-phase (air and slurry) flow, rather than three-phase (air, Therminol, and glass beads) flow is simulated. The apparent viscosity of the slurry phase is calculated by Einstein's viscosity for dilute suspension:

$$\mu^* = \mu\left(1 + \frac{5}{2}\alpha_s + O(\alpha_s^2)\right) \approx 1.08 \text{ cP} \tag{30}$$

The slurry density is calculated as

$$\rho^* = \alpha_s\rho_s + (1 - \alpha_s)\rho_t \approx 1015 \text{ kg/m}^3 \tag{31}$$

and the slurry phase surface tension is estimated as Therminol surface tension (17 dyn/cm). Values of the apparent density and viscosity of the slurry mixture are close to those of water, whereas its surface tension is much lower than that of water. The gas holdup profile is well predicted for both superficial gas velocity conditions.

In Figure 10, the time-and-azimuthally averaged liquid axial velocity and the phase-weighted liquid axial velocity are compared against each other as well as to CARPT data for the 44-cm column operated at U_g = 10 cm/s. The phase-weighted liquid axial velocity is defined as

$$\tilde{u}_{lz} = \frac{\overline{u_{lz}\alpha_l}}{\overline{\alpha_l}} \tag{32}$$

where $\bar{x}$ is the time-averaged value of the time series $x(t)$. It should be noted that the cross-sectional integral of the product of the time-averaged liquid axial velocity and the time-averaged liquid holdup is *not* equal to zero. Continuity requires

$$\langle\overline{\alpha_l(x, y, Z)u_{lz}(x, y, Z)}\rangle \equiv 0 \tag{33}$$

whereas

$$\langle\overline{\alpha_l(x, y, Z)u_{lz}(x, y, Z)}\rangle = \langle\overline{\alpha_l(x, y, Z)u_{lz}(x, y, Z)}\rangle + \langle\overline{\alpha_l'(x, y, Z)u_{lz}'(x, y, Z)}\rangle \tag{34}$$

and thus

$$\langle\overline{\alpha_l(x, y, Z)u_{lz}(x, y, Z)}\rangle = -\langle\overline{\alpha_l'(x, y, Z)u_{lz}'(x, y, Z)}\rangle \neq 0 \tag{35}$$

where $\langle\ \ \rangle$ is the cross-sectional integral, $\alpha_l'$and u_{lz}' are the gas holdup and liquid axial velocity fluctuations, respectively. From the simulated results, as shown in Figure 10, the difference between the time-averaged liquid velocity $\overline{u_{lz}}$ and phase-weighted liquid time-averaged velocity $\tilde{u}_{lz}$ is small. Thus the liquid holdup and velocity cross-correlation are not significant for the 44-cm-diameter column operated at U_g = 10 cm/s superficial gas velocity. The simulated $\overline{u_{lz}}$ value are higher than $\tilde{u}_{lz}$ value throughout the column, which indicates that the correlation between liquid holdup and axial velocity, $\langle\overline{\alpha_l'u_{lz}'}\rangle_s$, is negative. In other words, the correlation between *gas* holdup and *liquid* axial velocity, $\langle\overline{\alpha_g'u_{lz}'}\rangle_s$, is positive. This is consistent with the simulated time series of local gas holdup and liquid axial velocity, which is in-phase, as illustrated in Figure 4. The difference becomes smaller as one moves toward the wall region, where the gas holdup is lower and the fluctuation is not significant.

In Figure 11, the simulated time-and-azimuthally averaged gas holdup profiles, in a 16.2-cm-diameter air–water bubble column operated at U_g = 30 cm/s superficial gas velocity at 0.1, 0.4, and 1.0 MPa, are compared with CT experiments. The simulated results predict the gas holdup distribution well for all the operating pressures. One should note that to accomplish this favorable comparison we needed to weight the drag force by $(\rho_g/\rho_{g,0.1\text{MPa}})^{0.25}$, as indicated in Eq. 6. It seems that this

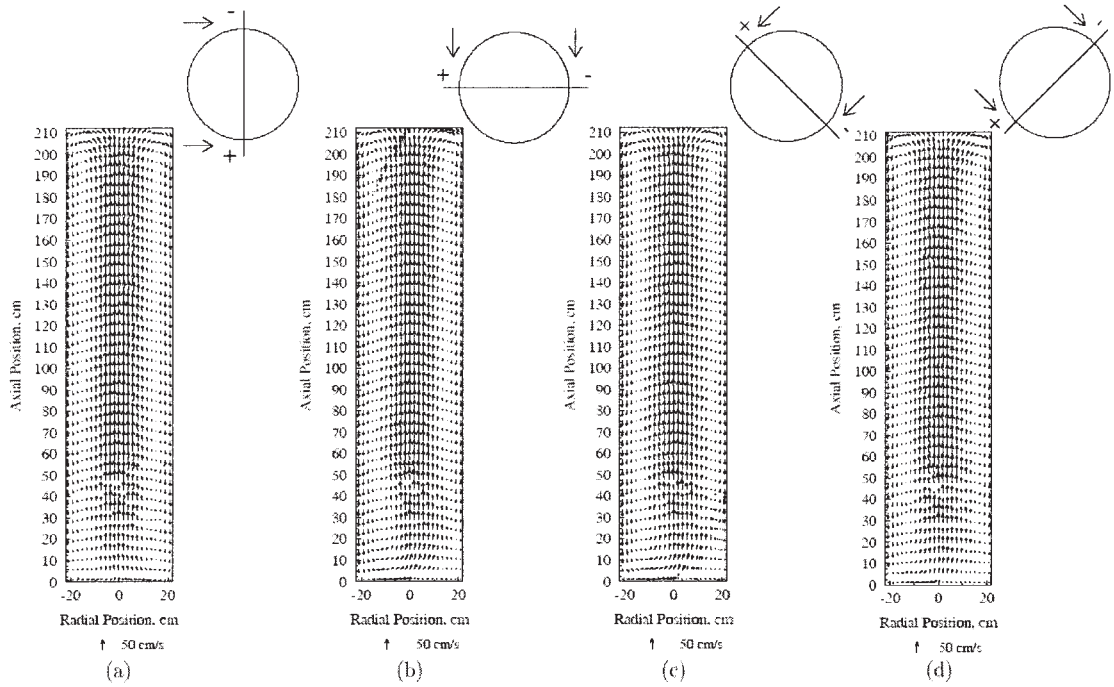

Figure 7. Velocity vector plot for D_C = 44 cm, U_g = 10.0 cm/s, P = 0.1 MPa (Degaleesan, 1997).

density correction factor used in this work, $(\rho_g/\rho_{g,0.1\text{MPa}})^{0.25}$, provides a good scaling factor for engineering purposes. However, the usefulness of this correction factor and the physical reasons for it need to be investigated further.

Figure 12 shows the time-and-azimuthally averaged axial liquid (water) velocity profiles and holdup weighted liquid (water) velocity profile in a 16.2-cm-diameter column at U_g = 30 cm/s superficial gas velocity and operated at 0.1, 0.4, and 1.0 MPa, respectively. From Table 3, it is evident that the cross-sectional integral of the product of simulated time-averaged liquid axial velocity and time-averaged liquid holdup, $\langle \overline{\alpha_l}\, u_{lz} \rangle_s$, has positive values, while the experimental one, $\langle \overline{\alpha_l\, u_{lz}} \rangle_e$, has negative values. The mass "imbalance" is negligible in 2-D axisymmetric simulation (Chen et al., 2005; Sanyal et al., 1999) because the axisymmetric boundary condition in 2-D computations causes the liquid flow to develop very quickly (5–10 s of real time) and reach its long-time "steady" pattern (Chen et al., 2005; Sanyal et al., 1999). In other words, the fluctuation of liquid holdup and axial velocity is artificially eliminated in such simulation. However, in reality and in 3-D simulations, such fluctuations can be significant at high superficial gas velocities (such as 30 cm/s). Figure 13 illustrates the model calculated cross-correlation of the liquid holdup and axial velocity, $-\overline{\alpha_l' u_{lz}'}$. The predicted magnitude of the liquid velocity and holdup cross-correlation increases with the gas superficial velocity, whereas it decreases with the operating pressure.

From the simulation, $\langle\, \overline{\alpha_l' u_{lz}'}\, \rangle_s$ is negative, which appears to be reasonable. Bubble column flow is buoyancy driven, gas

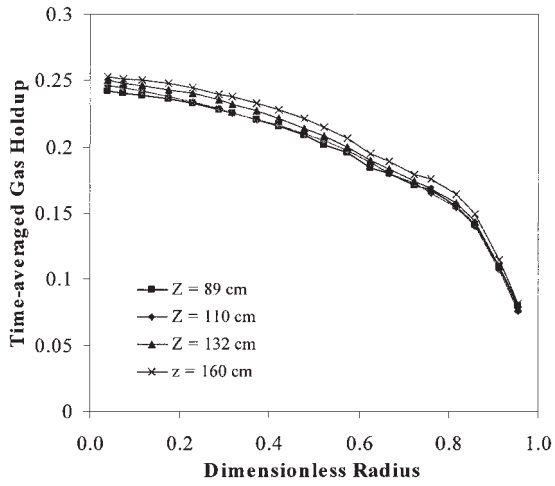

Figure 8. Time-averaged gas holdup profile evolution.

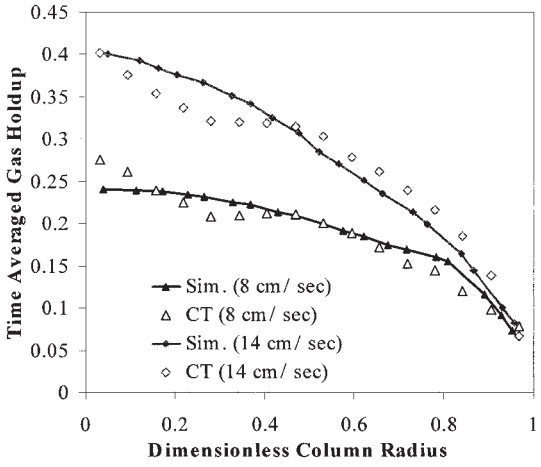

Figure 9. Comparison of time-averaged gas holdup profile of air–Therminol–glass beads system.

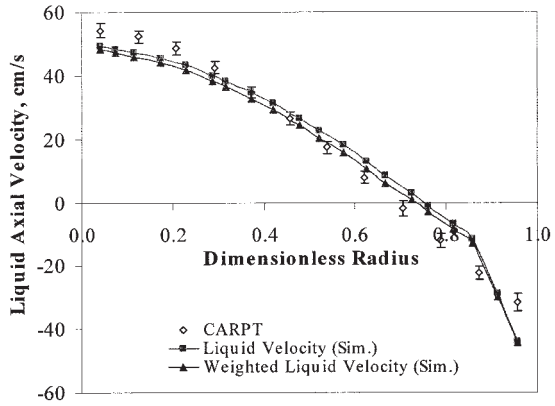

Figure 10. Comparison of time-averaged and liquid holdup weighted liquid axial velocity profile.

D_C = 44 cm, U_g = 10 cm/s, P = 0.1 MPa.

controls its hydrodynamics and momentum is transferred from the faster, upward moving, gas phase to the slower liquid phase. As a result, the time series of local gas holdup and liquid axial velocity should be in-phase, as illustrated in Figure 4. In other words, when $\alpha_g(\mathbf{x}, t = t_1) > \overline{\alpha_g}(\mathbf{x})$, the gas pocket will, most likely, bring liquid upward at a higher velocity than $\overline{u_{lz}}$ (see Figure 4). Thus, if $\alpha'_g > 0$ ($\alpha'_l < 0$), then $u'_{lz} > 0$, and thus $\alpha'_l u'_{lz} < 0$ (and $\overline{\alpha'_l u'_{lz}} < 0$) throughout the column, which is computed by the simulation and presented in Figures 10, 12, and 13, and Table 3. Moreover, the magnitude of $\langle \overline{\alpha'_l u'_{lz}} \rangle_s$ decreases with the operating pressure, which suppresses the chaotic nature of bubble column flows, as evident from both Table 3 and Figure 13.

However, the above analysis and simulation results are not in agreement with the data obtained from CARPT, from which $\langle \overline{\alpha'_l u'_{lz}} \rangle_e$ is indirectly estimated to be positive, suggesting that higher local instantaneous gas holdup is correlated with lower local liquid axial velocity. Moreover, the magnitude of $\langle \overline{\alpha'_l u'_{lz}} \rangle_e$ observed from experiments increases with the operating pressure, which suggests that higher operating pressure may *promote* the chaotic flow in bubble column. The experimental mass "imbalance" resulting from the average up-flow and down-flow rate shows little dependence on the operating pressure, whereas the operating pressure has a significant effect on simulated results as shown in Table 3. This discrepancy at the moment cannot be resolved and needs to be investigated in the future.

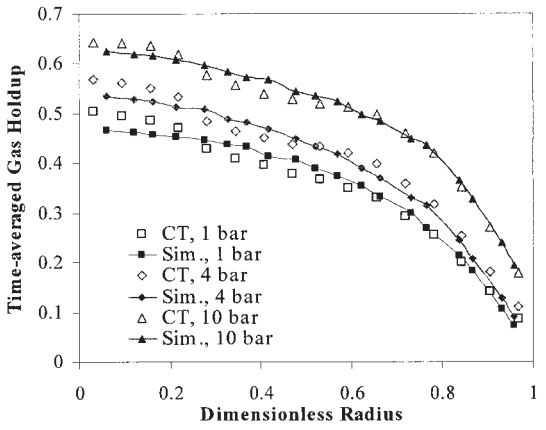

Figure 11. Comparison of time-averaged gas holdup profile obtained from simulations with experimental data (Ong, 2003) measured by CT technique for air–water bubble column.

D_C = 16.2 cm, U_g = 30 cm/s, P = 0.1, 0.4, and 1.0 MPa.

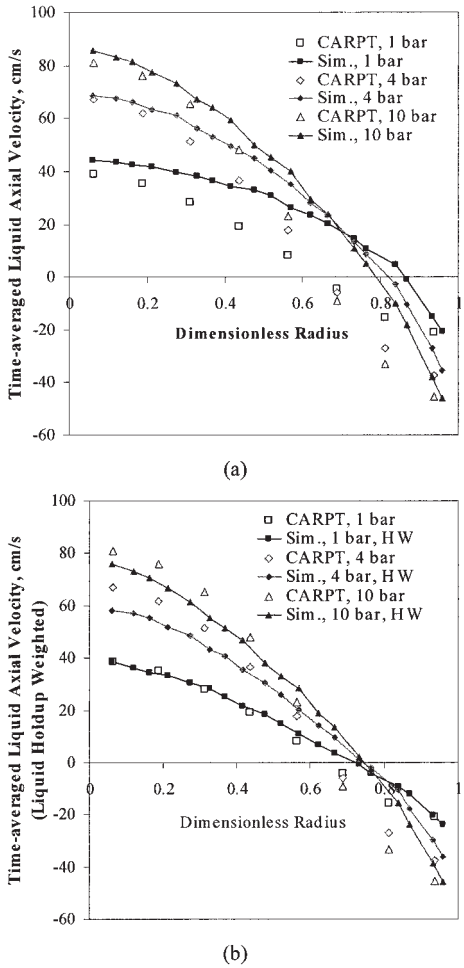

Figure 12. Comparison of liquid axial velocity profile obtained from simulations with experimental data (Ong, 2003) measured by CARPT technique for air–water bubble column.

D_C = 16.2 cm, U_g = 30.0 cm/s, P = 0.1, 0.4,, 1.0 MPa. (a) Time-averaged; (b) time-averaged and liquid holdup weighted.

In most current applications of bubble column CFD modeling, the full-scale simulations (that is, multiphase reacting flow

Table 3. Overall Liquid Continuity for Air–Water Bubble Column*

Pressure, P (MPa)	$\langle \overline{\alpha_l u_{lz}} \rangle$ (cm/s)	
	Exp.	Sim.
0.1	−3.3	6.8
0.4	−5.3	5.4
1.0	−6.7	2.7

*D_C = 16.2 cm and U_g = 30.0 cm/s.

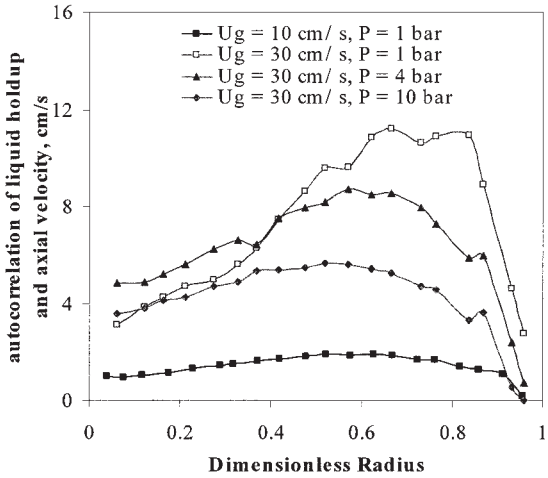

Figure 13. Cross-correlation radial distribution of the liquid holdup and axial velocity, $-\alpha_l' u_{lz}'$.

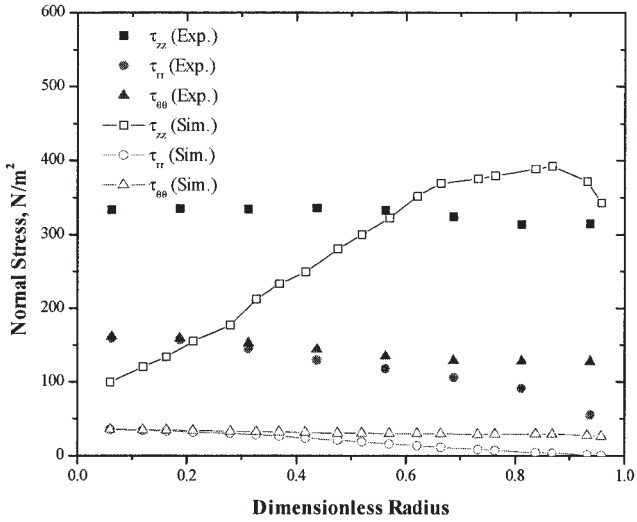

Figure 14. Comparison of the intensity of liquid turbulent normal stress obtained from simulations with experimental data (Ong, 2003) measured by CARPT technique for air–water bubble column.

D_C = 16.2 cm, U_g = 30.0 cm/s, P = 0.1 MPa.

simulations) are out of reach because of computational cost (20–30 scalar transport equations may need to be solved) instability, which arises from the nonlinear reaction rates (appearing in source term of scalar transport equation) and complicated reaction network. Thus, CFD is primarily used to provide the needed fluid dynamics to models ranging from the single-parameter axial dispersion model (Degaleesan and Duduković, 1998) to the 2-D convection with eddy-diffusion model (Degaleesan, 1997; Degaleesan et al., 1997). In these models, the preservation of the continuity condition for the gas and liquid phase is imperative. Moreover, it is the liquid flux, rather than liquid holdup or velocity itself, that matters in bubble column reactor modeling. Thus the holdup weighted liquid (water) velocity profile, $\bar{u}_{lz}(r)$, may need to be used for such purposes.

In addition to the mean axial liquid velocity profile, the intensities of fluctuations about the mean values are also provided by the CARPT experiments. Conventionally, these quantities, $\langle u_z' u_z' \rangle$, $\langle u_r' u_r' \rangle$, and $\langle u_\theta' u_\theta' \rangle$, as expressed in cylindrical coordinates, are called *turbulence intensities*. (Such a name may not be appropriate for the fluctuations arising from the periodic and/or quasi-periodic large-scale motions, which are usually not considered turbulence, and are included in these correlations. Nevertheless, the definition, mathematically, is clear.) The characteristics of the liquid phase motion are revealed, at first level, by these correlations.

Figure 14 compares the radial distribution of the liquid velocity autocorrelations calculated from the simulation, for a 16.2-cm-diameter air–water bubble column operated at 30 cm/s superficial gas velocity and 0.1 MPa, and those obtained from CARPT measurements. As expected, the values of the fluctuations in the axial direction are much stronger than those in the radial and angular directions. For the radial and angular normal stress, the numerical values are significantly lower than the experimental data. This is explained by the model's inability of resolving all the fluctuations as the turbulence level is enhanced by increasing the superficial gas velocity. For the axial normal stress, although the discrepancy between the simulated results and the experimental data is still significant, the relative difference is not as large as that for the radial and angular normal stress, and the difference becomes smaller as one moves toward the wall. In Figure 15, the liquid turbulent shear stress obtained from simulations is compared with experimental data. Similar to the prediction of normal stress in radial direction, the simulation significantly underpredicts the turbulent shear stress. Similar behavior was found in other simulations in this work. This comparison indicates and confirms that the present numerical model, although it can resolve the fluctuating liquid velocity in the bubbly flow regime, is not able to fully resolve

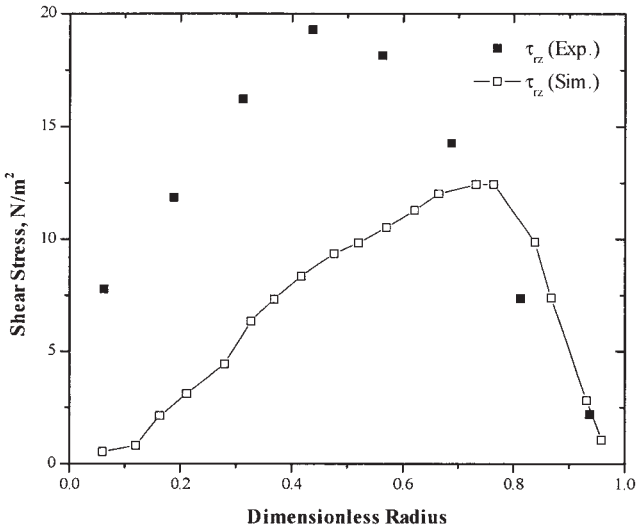

Figure 15. Comparison of the liquid turbulent shear stress obtained from simulations with experimental data (Ong, 2003) measured by CARPT technique for air–water bubble column.

D_C = 16.2 cm, U_g = 30.0 cm/s, P = 0.1 MPa.

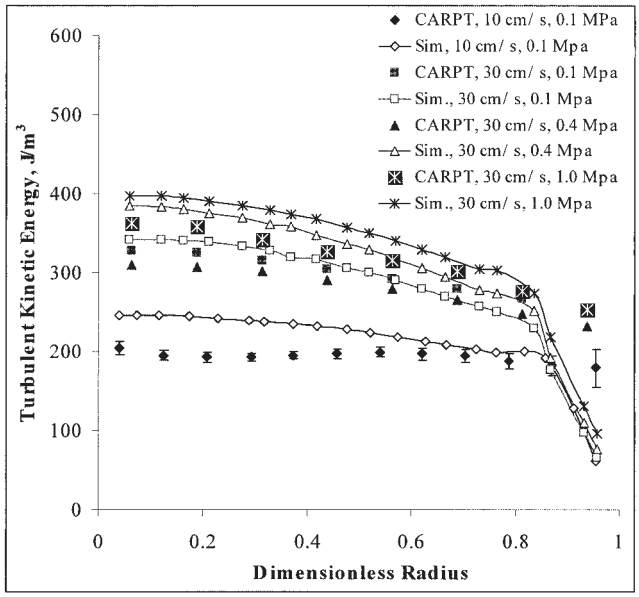

Figure 16. Comparison of the liquid turbulent kinetic energy obtained from simulations with experimental data (Chen et al., 1999; Ong, 2003) measured by CARPT technique for columns of different diameter and operated in the churn-turbulent regime.

the fluctuating liquid velocity in the churn-turbulent flow regime (Pan and Duduković, 2001).

Although the "turbulent" shear stress cannot be accurately predicted, the "turbulent" kinetic energy obtained from the k–ε model agrees reasonably well with the experimental data, as shown in Figure 16. One should note that in contrast to smaller diameter columns and operated at lower superficial gas velocity (such as $D_C = 14$ cm, $U_g = 9.6$ cm/s; and $D_C = 19$ cm, $U_g = 12.0$ cm/s), where kinetic energy profiles typically exhibit a maximum around the cross-over point for the time-averaged liquid axial velocity (Chen et al., 2005; Degaleesan, 1997), such a peak does not exist in bigger columns ($D_C = 44$ cm) or at higher superfical gas velocity ($U_g = 30$ cm/s).

Figure 17 shows the simulated time-and-azimuthally averaged volume fraction profiles for different diameter bubbles in a 16.2-cm-diameter air–water bubble column operated at 30 cm/s superficial gas velocity and 0.1 MPa. The volume fraction of small bubbles ($d \leq 4$ mm) is uniformly distributed, especially for tiny bubbles ($d < 2.5$ mm). For large bubbles, however, the volume fraction distribution peaks in the center as shown in Figure 17b. In Figure 18, the effects of operating pressure and velocity on medium diameter bubbles are illustrated. The radial holdup distributions of such bubbles are more uniform at higher pressure (1.0 MPa) than those at lower pressure (0.1 MPa), which indicates that the simulation correctly captured the pressure effect on bubble column flow, which pushes the churn-turbulent flow toward bubbly flow when the pressure is increased.

In Figure 19, the simulated cumulative bubble volume fraction is given. The summation of the volume fraction of all bubble classes is equal to the simulated gas holdup; thus, if the simulated overall gas holdup is underestimated, the cumulative

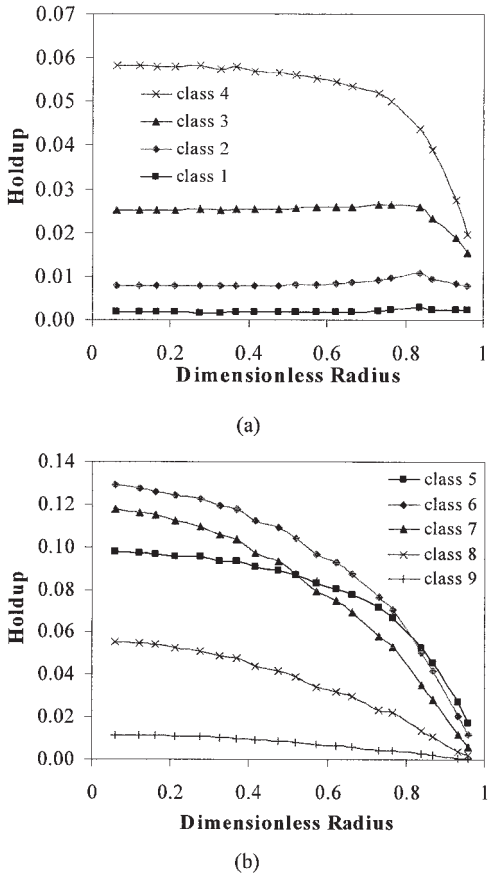

Figure 17. Time-averaged bubble class holdup profile.

$D_C = 16.2$ cm, $U_g = 30.0$ cm/s, $P = 0.1$ MPa.

bubble volume fraction will most likely be underestimated as well. Similarly, if the simulated overall gas holdup is overestimated, the cumulative bubble volume fraction will also most likely be overestimated. Thus, for fair comparison, each bubble

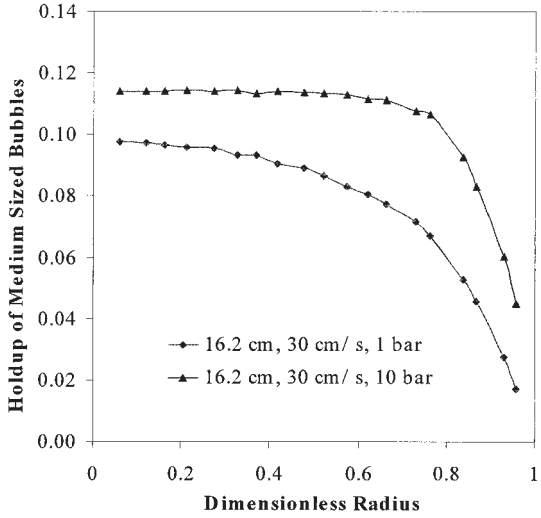

Figure 18. Effect of operating pressure on medium-size bubbles.

$d = 6.35$ mm.

class volume fraction needs to be weighted against the experimental gas holdup. This weighting procedure can be written as

$$\bar{\alpha}_{i,adj} = \bar{\alpha}_{i,sim} \frac{\bar{\alpha}_{g,\exp}}{\bar{\alpha}_{g,sim}} \tag{36}$$

Here, we made the assumption that the increase/decrease of overall gas holdup would not change the bubble volume fraction based distribution. Because the relative error of the simulation against the experimental overall gas holdup, as well as the adjusting factor, is small (see Table 1), it may be a valid assumption. It can be seen that the cumulative volume fraction of smaller bubbles (up to 6.4 mm) does not change with the superficial gas velocity (10 and 30 cm/s), whereas it increases with respect to the operating pressure, which it is in line with the two-bubble-class hypothesis (for example, Krishna and Ellenberger, 1996). Nevertheless, a bimodal bubble size distribution is not found in the simulation, as shown in Figure 20. The operating pressure does not have a noticeable effect on the simulated bubble size distribution, which results from breakup and coalescence closures used in this work that do not take the pressure effect into account. The superficial gas velocity has little effect on volume fraction of small bubbles (1 and 1.6 mm), whereas such an effect becomes pronounced for larger bubbles. The bubble size distribution becomes wider and the Sauter mean bubble diameter becomes larger as the superficial gas velocity increases. The simulation suggests that, although the volume fraction of small bubbles may not change with respect to the superficial gas velocity in churn-turbulent flow regime, the bubble size distribution could still remain single modal and simply become wider and move toward larger bubble diameter when the superficial gas velocity increases. Rigorous measurements of bubble size distribution in churn-turbulent flow, such as possibly by the four-point optical probe, are needed to clarify these issues.

Summary and Conclusions

The numerical simulation of the transient gas–liquid flow in three-dimensional cylindrical bubble columns, using the Euler/Euler two-fluid model (TFM) and the ASMM with BPBE implemented, is able to capture the dynamic features of large-scale structures. The time-averaged liquid velocity field exhibits single-loop axisymmetric recirculation pattern in the middle section of the column. Such a flow pattern was previously confirmed experimentally by liquid velocity measurements, which used the computer-automated radioactive particle tracking (CARPT) technique, in various columns operating at churn-turbulent flow conditions. The evidence, both numerical and experimental, supports the assumption of one-dimensionality of the time-averaged velocity profile, in the sense of time- and azimuthal-averaging, within the middle section of the column and, in turn, the use of 1-D recirculation model widely adopted in engineering applications (Degaleesan, 1997). Quantitative comparisons with the experimental (CT/CARPT) data demonstrate that, by applying interphase momentum transfer, modified k–ε turbulence model in the liquid phase, and the BPBE for the bubble size prediction, the two-fluid and ASMM simulations are able to provide satisfactory a mean axial liquid velocity and gas radial holdup profile for columns operated over a wide range of superficial velocity, operating pressure, physical properties, and column diameter. By comparing the computed and experimentally determined turbulence intensities (autocorrelations of the liquid velocity fluctuations) and the Reynolds shear stress (cross-correlation of the liquid velocity fluctuations), we find that for columns operating in the churn-turbulent regime the velocity field cannot be fully resolved, resulting in an underestimated prediction of the fluctuation-related mean quantities. The simulation correctly captured qualitatively the elevated pressure effect on bubble column flows, which pushes the churn-turbulent flow toward bubbly flow when the pressure is increased, suggesting that although the volume fraction of small bubbles may not change with respect to the superficial gas velocity in churn-turbulent flow regime, the bubble size distribution still remains single modal but becomes wider and moves toward larger bubble diameter when the superficial gas velocity is increased. For truly predictive results in simulation of gas–liquid flows in a churn-turbulent regime, further investigations are needed to explore the models for momentum exchange, bubble breakup/coalescence, and the models for multiphase turbulence.

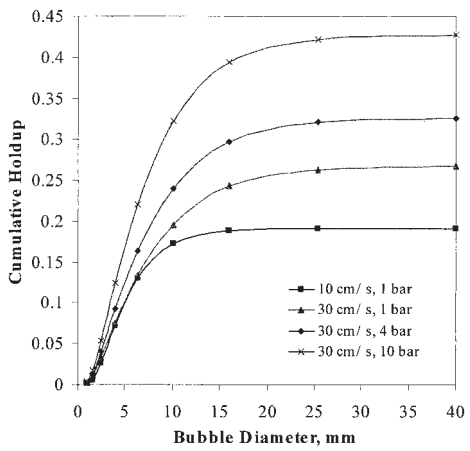

Figure 19. Overall bubble classes cumulative holdup.

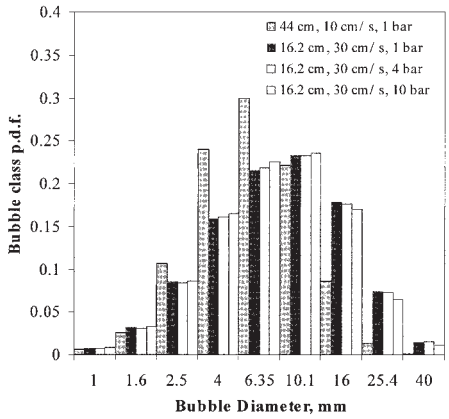

Figure 20. Bubble classes holdup-based probability distribution.

Acknowledgments

Two of the authors (P. Chen and M. P. Duduković) acknowledge the support of the industrial sponsors of the Chemical Reaction Engineering

Laboratory (CREL). We express our sincere appreciation to Dr. S. Vasquez of Fluent, Inc. for formulating the original multiphase model in Fluent v6.

Notation

a = breakup frequency, s^{-1}
b = coalescence frequency, s^{-1}
c = dimensionless constant in Eq. 25, $c = 0.4$
c_B = dimensionless constant in Eq. 23, $c_B \approx 0.923$
C_D = drag coefficient, dimensionless
c_f = increase coefficient of surface area, $c_f = f_{BV}^{2/3} + (1 + f_{BV})^{2/3} - 1$
d, d_B = bubble diameter, m
d_h = sparger orifice diameter, m
d_s = bubble diameter at the sparger, m
f = bubble number density function
f_{BV} = volume fraction of one daughter bubble, dimensionless
$\mathbf{F}_{kl}$ = interfacial momentum exchange term, N m^{-3}
$\mathbf{g}$ = gravity, m^2 s^{-1}
$\mathbf{M}_d$ = drag force per unit volume, N m^{-3}
n, N = number density of bubble class, m^{-3}
N_w = in Eq. 29, $N_w = \mathrm{We}/\mathrm{Fr}^{1/2} = d_o^{1.5} U_{gh} \rho_l g^{0.5}/\sigma$
P = pressure, Pa
P_C = coalescence efficiency, dimensionless
Re = bubble Reynolds number, dimensionless, $\mathrm{Re} = d_b \left| \mathbf{u_l} - \mathbf{u_g} \right| \rho_l / \mu_l$
S = source term, s^{-1}
S_i = source term, m^{-3} s^{-1}
$\bar{u}_i$, $\bar{u}_j$ = bubble velocity in turbulence, m/s
$\bar{u}_{ij}$ = bubble approaching velocity in turbulence, m/s
$\mathbf{u}$ = velocity, m/s
$\mathbf{u}'$ = velocity fluctuation, m/s
v = bubble volume, m^3
U_g = superficial gas velocity, m/s
U_{gh} = gas velocity at the sparger holes, m/s
t = time, s
We = Weber number, dimensionless
$\mathbf{x}$ = position vector
x_i = diameter of ith bubble tracked in BPBE, m

Greek letters

α = void fraction, dimensionless
β = dimensionless constant in Eq. 23
ε = dissipation rate, m^2/s^3
γ = fraction that to be reassigned to nearby bubble classes, dimensionless
λ = arriving eddy size, m
μ = dynamic viscosity, kg m^{-1} s^{-1}
$\pi_{i,j}$ = defined in Eq. 28
θ = collision frequency, m^{-3} s^{-1}
ρ = density, kg/m^3
σ = surface tension, kg s^{-2}
τ = shear stress tensor
Ω_B = breakup rate, m^{-3} s^{-1}
ξ = d_i/d_j or λ/d, dimensionless

Subscripts

b = bubble
c = continuous phase
d = dispersed Phase
g = gas phase index
i, j = bubble class index
k = phase index
l = liquid phase index
p = particle
r = reaction

Superscripts

i = bubble class index
p = pressure change
ph = phase change

Literature Cited

Chaouki, J., F. Larachi, and M. P. Duduković, *Non-Invasive Monitoring of Multiphase Flows*, p. 585, Elsevier, Amsterdam (1997).

Chen, J., F. Li, S. Degaleesan, P. Gupta, M. H. Al-Dahhan, M. P. Duduković, and B. A. Toseland, "Fluid Dynamic Parameters in Bubble Columns with Internals, " *Chem. Eng. Sci.*, **54**(13–14), 2187 (1999).

Chen, P., J. Sanyal, and M. P. Duduković, "Numerical Simulation of Bubble Columns Flows: Effect of Different Breakup and Coalescence Closures, " *Chem. Eng. Sci.*, **60**(4), 1085 (2005).

Clift, R., J. R. Grace, and M. E. Weber, *Bubbles, Drops and Particles*, Academic Press, New York (1978).

Degaleesan, S., "Fluid Dynamic Measurements and Modeling of Liquid Mixing in Bubble Columns," DSc Thesis, Washington University, St. Louis, MO (1997).

Degaleesan, S., and M. P. Duduković, "Liquid Backmixing in Bubble Columns and the Axial Dispersion Coefficient," *AIChE J.*, **44**(11), 2369 (1998).

Degaleesan, S., M. P. Duduković, B. A. Toseland, and B. L. Bhatt, "A Two-Compartment Convective–Diffusion Model for Slurry Bubble Column Reactors," *Ind. Eng. Chem. Res.*, **36**(11), 4670 (1997).

Delnoij, E., F. A. Lammers, J. A. M. Kuipers, and W. P. M. van Swaaij, "Dynamic Simulation of Dispersed Gas–Liquid Two-Phase Flow Using a Discrete Bubble Model," *Chem. Eng. Sci.*, **52**(9), 1429 (1997).

Devanathan, N., "Investigation of Liquid Hydrodynamics in Bubble Columns via Computer Automated Radioactive Particle Tracking (CARPT)," DSc Thesis, Washington University, St. Louis, MO (1991).

Devanathan, N., D. Moslemian, and M. P. Duduković, "Flow Mapping in Bubble Columns Using CARPT," *Chem. Eng. Sci.*, **45**, 2285 (1990).

Drew, D. A., "Mathematical Modeling of Two-Phase Flow," *Ann. Rev. Fluid Mech.*, **15**, 261 (1983).

Drew, D. A., and S. L. Passmann, *Theory of Multicomponent Fluids*, Springer-Verlag, New York (1999).

Elghobashi, S. E., and T. W. Abou-Arab, "A Two-Equation Turbulence Model for Two-Phase Flows," *Phys. Fluids*, **26**(4), 931 (1983).

George, D. L., K. A. Shollenberger, and J. R. Torczynski, "Sparger Effect on Gas Volume Fraction Distributions in Vertical Bubble-Column Flows as Measured by Gamma-Densitometry Tomography," *Proc. of ASME 2000 Fluids Engineering Division Summer Meeting*, p. 471, Boston, MA (2000).

Ishii, M., and N. Zuber, "Drag Coefficient and Relative Velocity in Bubbly, Droplet, or Particulate Flows," *AIChE J.*, **25**(5), 843 (1979).

Jakobsen, H. A., B. H. Sannaes, S. Grevskott, and H. Svendsen, "Modelling of Vertical Bubble-Driven Flows," *Ind. Eng. Chem. Res.*, **36**, 4052 (1997).

Jenne, M., "Modellierung und Simulation der Strömungsverhältnisse in begasten Rührkesselreaktoren," Dissertation, Universität Stuttgart, Germany (1999).

Kashiwa, B. A., and R. M. Rauenzahn, "A Multimaterial Formalism," *FED* (*Am. Soc. Mech. Eng.*), **185**, 149 (1994).

Krishna, R., and J. Ellenberger, "Gas Holdup in Bubble Column Reactors Operating in the Churn-Turbulent Flow Regime," *AIChE J.*, **42**, 2627 (1996).

Krishna, R., and J. M. van Baten, "Eulerian Simulations of Bubble Columns Operating at Elevated Pressures in the Churn Turbulent Flow Regime, " *Chem. Eng. Sci.*, **56**(21–22), 6249 (2001).

Krishna, R., J. M. van Baten, and M. I. Urseanu, "Three-Phase Eulerian Simulations of Bubble Column Reactors Operating in the Churn-Turbulent Regime: A Scale-up Strategy, " *Chem. Eng. Sci.*, **55**(16), 3275 (2000).

Kumar, S., and D. Ramkrishna, "On the Solution of Population Balance Equations by Discretization—I. A Fixed Pivot Technique," *Chem. Eng. Sci.*, **51**, 1311 (1996).

Kumar, S. B., "Computed Tomographic Measurements of Void Fraction and Modeling of the Flow in Bubble Columns," PhD Thesis, Florida Atlantic University, Boca Raton, FL (1994).

Kumar, S. B., D. Moslemian, and M. P. Duduković, "A Gamma-Ray Tomographic Scanner for Imaging Voidage Distribution in Two-Phase Flow Systems," *Flow Meas. Instrum.*, **6**(1), 61 (1995).

Kumar, S. B., D. Moslemian, and M. P. Duduković, "Gas-Holdup Mea-

surements in Bubble Columns Using Computed Tomography," *AIChE J.*, **43**(6), 1414 (1997).
Lahey, R. T., "The Analysis of Phase Separation and Phase Distribution Phenomena Using Two-Fluid Model, " *Adv. Nucl. Eng. Des.*, **122**, 17 (1990).
Lapin, A., and A. Lübbert, "Numerical Simulations of the Dynamics of Two-Phase Gas–Liquid Flows in Bubble Columns," *Chem. Eng. Sci.*, **49**(21), 3661 (1994).
Launder, B. E., and D. B. Spalding, *Mathematical Models of Turbulence*, Academic Press, London (1974).
Letzel, H. M., J. C. Schouten, C. M. van den Bleek, and R. Krishna, "Influence of Gas Density on the Large-Bubble Holdup in Bubble Column Reactors," *AIChE J.*, **44**, 2333 (1998).
Luo, H., "Coalescence, Breakup and Liquid Circulation in Bubble Column Reactors," PhD Thesis, Norwegian Institute of Technology, Trondheim, Norway (1993).
Luo, H., and H. F. Svendsen, "Theoretical Model for Drop and Bubble Breakup in Turbulent Dispersions," *AIChE J.*, **42**, 1225 (1996).
Miyahara, T., Y. Matsuba, and T. Takahashi, "The Size of Bubbles Generated from Perforated Plates, " *Int. Chem. Eng.*, **23**(3), 517 (1983).
Moslemian, D., N. Devanathan, and M. P. Duduković, "Radioactive Particle Tracking Technique for Investigation of Phase Recirculation and Turbulence in Multiphase Systems," *Rev. Sci. Instrum.*, **63**(10), 4361 (1992).
Oey, R. S., R. F. Mudde, and H. E. A. Van den Akker, "Sensitivity Study on Interfacial Closure Laws in Two-Fluid Bubbly Flow Simulations, " *AIChE J.*, **49**(7), 1621 (2003).
Ong, B., "Experimental Investigation of Bubble Column Hydrodynamics—Effect of Elevated Pressure and Superficial Gas Velocity," DSc Thesis, Washington University, St. Louis, MO (2003).
Pan, Y., and M. P. Duduković, "Mean Axial Liquid Velocity Profiles in Bubble Columns—Numerical versus CARPT," *Proc. of the Annual Meeting of Chemical Reaction Engineering Laboratory* (*CREL*), Washington University, St. Louis, MO (2000).
Pan, Y., and M. P. Duduković, "CFD Simulations of a Bubble Column—2-D versus 3-D," *Proc. of 6th World Congress of Chemical Engineering*, Melbourne, Australia, Sep. 23–27 (2001).
Pan, Y., M. P. Duduković, and M. Chang, "Dynamic Simulation of Bubbly Flow in Bubble Columns," *Chem. Eng. Sci.*, **54**, 2481 (1999).
Pan, Y., M. P. Duduković, and M. Chang, "Numerical Investigation of Gas-Driven Flow in 2-D Bubble Columns," *AIChE J.*, **46**(3), 434 (2000).
Pfleger, D., S. Gomes, N. Gilbert, and H. G. Wagner, "Hydrodynamics Simulations of Laboratory Scale Bubble Columns Fundamental Studies of the Eulerian–Eulerian Modelling Approach, " *Chem. Eng. Sci.*, **54**, 5091 (1999).
Rafique, M., P. Chen, and M. Duduković, "Computational Modeling of Gas–Liquid Flow in Bubble Columns," *Rev. Chem. Eng.*, **20**(3–4), 225 (2004).
Ranade, V. V., and Y. Tayalia, "Modelling of Fluid Dynamics and Mixing in Shallow Bubble Column reactors: Influence of Sparger Design," *Chem. Eng. Sci.*, **56**, 1667 (2001).
Roy, S., "Quantification of Two-Phase Flow in Liquid–Solid Risers," DSc Thesis, Washington University, St. Louis, MO (2000).
Saffman, P. G., and J. S. Turner, "On the Collision of Drops in Turbulent Clouds," *J. Fluid Mech.*, **1**, 16 (1956).
Sanyal, J., S. Vasques, S. Roy, and M. P. Duduković, "Numerical Simulations of Gas–Liquid Dynamics in Cylindrical Bubble Column Reactors," *Chem. Eng. Sci.*, **54**, 5071 (1999).
Schiller, L., and Z. Z. Naumann, "Über die grundlegenden Berechungen bei der schwerkraftaufbereitung," *Ver. Deutsch. Ing.*, 77–318 (1935).
Schwarz, M. P., and W. J. Turner, "Applicability of Standard k–ε Turbulence Model to Gas Stirred Bath," *Appl. Math. Model.*, **12**, 273 (1988).
Shaikh, A, Rados, N, Al-Dahhan, MH. "Phase Distribution in a High Pressure Slurry Bubble Column via Computed Tomography," *Proc. of the 4th Middle East Refining and Petrochemical Exhibition and Conference*, PetroTech 2003, Manama, Bahrain, Sep. 28–Oct. 1 (2003).
Shollenberger, K. A., D. L. George, and J. R. Torczynski, *Effect of Sparger Geometry on Gas-Volume-Fraction in Bubble-Column Flows Measured by Gamma-Densitometry Tomography* (*GDT*), Sandia National Laboratories, Livermore, CA (2000).
Sokolichin, A., and G. Eigenberger, "Gas–Liquid Flow in Bubble Columns and Loop Reactors: Part I. Detailed Modelling and Numerical Simulation," *Chem. Eng. Sci.*, **49**(24B), 5735 (1994).
Tchen, C. M., "Mean Value and Correlation Problems Connected with the Motion of Small Particles Suspended in a Turbulent Fluid," PhD Thesis, Technische Universiteit Delft, The Netherlands (1947).
Torvik, R., and H. F. Svendsen, "Modeling of Slurry Reactors: A Fundamental Approach, " *Chem. Eng. Sci.*, 45, 2325 (1990).
Tsuchiya, K., A. Furumoto, L. S. Fang, and J. Zhang, "Suspension Viscosity and Bubble Rise Velocity in Liquid–Solid Fluidized Beds, " *Chem. Eng. Sci.*, **52**, 3053 (1997).
van Baten, J. M., and R. Krishna, "Eulerian Simulations for Determination of the Axial Dispersion of Liquid and Gas Phases in Bubble Columns Operating in the Churn-Turbulent Regime," *Chem. Eng. Sci.*, **56**(2), 503 (2001).
Yang, Y. B., N. Devanathan, and M. P. Duduković, "Liquid Backmixing in Bubble Columns," *Chem. Eng. Sci.*, **47**(9–11), 2859 (1992).
Zhang, D. Z., and A. Prosperetti, "Momentum and Energy Equations for Disperse Two-Phase Flows and Their Closure for Dilute Suspensions," *Int. J. Multiphase Flow*, **23**(3), 425 (1997).

Manuscript received Jan. 16, 2004, and revision received July 9, 2004.